Research Square

Preprints are preliminary reports that have not undergone peer review.
They should not be considered conclusive, used to inform clinical practice,
or referenced by the media as validated information.

Flexible Nitrogen-doped Carbon Networks of Fe 0.64 Ni 0.36 Nanocomposites as Anode Materials for High-performance Lithium-ion Batteries

Rongbin Yao
Lianyungang Normal University
Chengxiang Sun
chengxsun@hhu.edu.cn
Lianyungang Normal University
Mianyi Wang
Lianyungang Normal University
Yuhang Zheng
State Grid Jiangsu Electric Power Engineering Consulting Co., Ltd
Jinli Li
Lianyungang Normal University
Jianhong Zhu
Hohai University
Cheng Liu
Zhejiang University
Gengtao Guo
NARI Technology Co., Ltd
Dianyuan Zheng
Lianyungang Normal University

Research Article

Keywords: Nitrogen-doped carbon, Fe0.64Ni0.36 nanoparticles, Lithium ion batteries anode, Electrochemical Performance, Chitosan

Posted Date: May 20th, 2026

DOI: https://doi.org/10.21203/rs.3.rs-9508769/v1

License: This work is licensed under a Creative Commons Attribution 4.0 International License.
Read Full License

Additional Declarations: No competing interests reported.

Abstract

Binary transition metal compounds-based anodes for lithium-ion batteries hold great promise, yet they still face stumbling blocks due to the issues including poor electrical conductivity and large volume expansion during lithium-ion insertion. In this work, we report a facile and innovative strategy to relieve the mechanical strain of FeNi oxide nanoparticles via encapsulation within heteroatom-doped honeycomb-like carbon layers. The design effectively enhances the stability of electrode-electrolyte interphase. FeNi oxide nanoparticles were coated with a carbon layer integrated with nitrogen using carboxymethyl chitosan obtained from chitosan under microwave irradiation, followed by carbonization, resulting in the $Fe_{0.64}Ni_{0.36}$@C-N nanocomposite. The heteroatom doping perturbs the carbon lattice, creating defects, vacancies, and functional groups that act as active sites for Li^+ adsorption and facilitate ion diffusion. The porous carbon layer facilitates efficient electrolyte penetration and mitigates volume changes upon cycling. Typically, the engineered $Fe_{0.64}Ni_{0.36}$ nanocomposite anode (FN6) with a CMCS content of 6 mol L^{-1} displays the best rate performances, with a high reversible capacity of 890 mAh g^{-1} at a current density of 0.05 A g^{-1}. The FN6 also exhibits 740 and 585 mAh g^{-1} at 0.5 and 1.0 A g^{-1}, respectively, while maintaining a coulombic efficiency over 99.89% for 80 cycles. Additionally, the FN14 (with a CMCS content of 14 mol L^{-1}) exhibit exceptional cycling performance after 1 000 cycles. This work presents a new way to optimize anode materials for high-performance lithium-ion batteries.

1. INTRODUCTION

The rapid development of electric vehicles highlights the urgent need for lithium-ion batteries (LIBs) with high energy density, high power density, and extended cycle life[1, 2, 3]. Nickel-iron (Ni-Fe) based metal compounds have been regarded as promising anode materials for LIBs, which have drawn extensive scientific interest due to their superior corrosion resistance and high theoretical capacity[4, 5]. Nevertheless, their application faces challenges, including large volume expansion and poor rate capability during the charge and discharge cycling[6].

In recent years, many researchers have focused on enhancing the electrochemical performance of Ni-Fe compounds via various innovative strategies. Carbon coating, for instance, enhances cycling stability and alleviates volume change effects in nanostructured Ni-Fe anodes[7]. For instance, Christie Thomas et al. synthesized carbon-coated $NiFe_2O_4$ nanofibers via electrospinning, which displayed superior cycling stability as well as a high specific capacity of 870 mAh g^{-1}; the carbon coating boosted conductivity and the overall electrochemical performance[8].

Another key strategy is surface decoration of carbon materials, which preserves their high specific surface area by suppressing the restacking of metal nanoparticles. The synergistic integration of high-capacity transition metal nanoparticles with high specific surface area and superior electrical conductivity of carbon matrices markedly enhances cycling stability, rate capability, and energy storage performance[9, 10]. Many studies have employed xylene, benzyl alcohol, naphthalene, and phenyl

phosphate as derivative linkers to encapsulate nanoparticles within carbon nanotubes[11, 12]. Introducing S and N promotes the generation of C–S and C–N chemical bonds, distorting crystal lattice and enhancing local chemical activity. Moreover, heteroatom (S, N) doping of carbon frameworks effectively boosts electrical conductivity and creates abundant active sites for Li^+storage. These defect-rich carbon substrates expose more active sites than pristine carbon, thereby accelerating electrochemical kinetics. Additionally, minimizing the interface gap between metal particles and carbon substrates enables more efficient accommodation of volume expansion during cycling, thus enhancing structural stability[13].

While carbon coatings effectively mitigate electrode degradation by forming stable chemical bonds, the development of next-generation carbon frameworks remains essential for enhancing the overall electrochemical performance. These advanced structures must simultaneously protect metal components, enhance electrical conductivity, and provide abundant active sites to improve Li^+storage capacity, thus achieving an excellent balance between the structural stability and high specific capacity of electrode materials[14, 15, 16, 17, 18]. Based on previous studies, we infer that the capacity stability of $Fe_{0.64}Ni_{0.36}$ requires effective carbon coating via nitrogen-doped soft carbon, as well as strong interparticle connectivity to maintain a conductive network during cycling. This connectivity can be achieved by synthesizing a structurally robust composite—such as $Fe_{0.64}Ni_{0.36}$ embedded in porous carbon derived from chitosan—or by incorporating the active material into a carbon nanofiber or nanotube matrix.

In this work, the nitrogen-doped carbon-coated $Fe_{0.64}Ni_{0.36}$ nanoparticles ($Fe_{0.64}Ni_{0.36}$@C-N) were synthesized by a low-cost sol-gel method. This material exhibits superior electrochemical performance compared to its CMCS. The 15 nm carbon coating not only affords robust protection to the $Fe_{0.64}Ni_{0.36}$ nanoparticles against volume expansion and particle aggregation but also integrates nitrogen doping into its framework. This dual functionality synergistically increases the defect density and exposes abundant active sites, thereby significantly accelerating lithium-ion (Li^+) transport kinetics and improving interfacial charge transfer efficiency. Comparative analysis reveals the $Fe_{0.64}Ni_{0.36}$@C-N anode delivers an exceptional specific capacity of 890 mAh g^{-1} at 0.05 A g^{-1}, markedly higher than that of the CMCS anode (205 mAh $g^{-1)}$. The FN14 while maintaining excellent cycling stability with no obvious capacity decay over 1000 cycles of charge-discharge. Nitrogen doping in the carbon framework significantly improves electronic conductivity and boosts Li^+adsorption capability by forming the Li-N chemical bonds, which directly mitigates the key limitations identified in previous studies. Experimental results further corroborate these findings, demonstrating that doped nitrogen enhances the binding energy of Li^+ ions on the $Fe_{0.64}Ni_{0.36}$@C-N surface, providing mechanistic insight into the performance enhancement. This study demonstrates the efficacy of nitrogen-doped carbon coatings in mitigating volume expansion of $Fe_{0.64}Ni_{0.36}$ anodes and presents a straightforward method for developing stable, high-performance LIB materials. Nitrogen doping within the carbon framework remarkably boosts the Li^+adsorption capacity and enhances electronic conductivity through the formation of Li-N chemical bonds.

2. EXPERIMENTAL SECTION

2.1 Chemicals. Chemicals purchased from the National Pharmaceutical Group of China (Shanghai), including analytical grade $FeCl_3 \cdot 6H_2O$, $NiCl_2 \cdot 6H_2O$, acetic acid, anhydrous ethanol and acetone, were used as received without further purification. Jiangsu Xianfeng Nanometer Co., Ltd. (Nanjing) provided the chitosan (Sigma, Deacetylation > 75%, Viscosity 20–300 cps).

2.2 Material Synthesis. Based on our previous research[13], carboxymethyl chitosan (CMCS) was synthesised as follows: First, 3.0 g of chitosan was made more alkaline by stirring it in 4.0 ml of a 50 wt% sodium hydroxide solution for 30 minutes. Then, 15.0 g of monochloroacetic acid was incorporated into the mixture, followed by stirring in a water bath at 90°C for an additional 30 minutes to ensure thorough homogenisation. Finally, the pH was adjusted to 7 by gradually adding glacial acetic acid[19]. Electrode material preparation was optimized based on previous methods[20]. $Fe_{0.64}Ni_{0.36}$@C-N was typically synthesized by dispersing $NiCl_2 \cdot 6H_2O$ (0.01mol L^{-1}), $FeCl_3 \cdot 6H_2O$ (0.02 mol L^{-1}), 10 mol L^{-1} CMCS(calculated as monosaccharides), and in 100 mL water, followed by 30 minutes of sonication and magnetic stirring for homogenization, then the samples were further subjected to microwave treatment. The mixture was annealed under an argon atmosphere at approximately 800°C (temperature rise rate: 2°C min^{-1}) to yield $Fe_{0.64}Ni_{0.36}$@C-N. For the control sample carboxymethyl chitosan were treated identically and labelled CMCS for comparative purposes.

2.3 Material Characterization. The crystal structure of samples was recorded by an X-ray diffractometer (XRD, Rigaku MiniFlex600-C) with Cu-Kα radiation (λ = 1.5406 Å). Raman scattering spectra were performed with HORIBA system, using a 532 nm Ar^+ laser. The microstructure and morphology of composites were detected with a field emission scanning electron microscope (SEM, HITACHI S-4800, Japan) and transmission electron microscopy (TEM, FEI Tecnai G2 F20 microscope, USA). XPS analysis was performed with Al Kα monochromatic radiation (hν = 1486.6 eV) on an Escalab 250Xi photoelectron spectrometer (USA).

2.4 Electrode Preparation and Electrochemical Measurement. The sample slurry was prepared by suspending an active material (80 wt%), a polyvinylidene fluoride (PVDF) binder (10 wt%) and a carbon black (CB) conductive additive (10 wt%) in N-methyl-2-pyrrolidone (NMP). The slurry was then uniformly coated onto a copper foil (1.2 cm in diameter), dried at 80°C for three hours and vacuum-dried for a further 12 hours. The amount of active material loaded was determined by weighing each electrode individually. The electrolyte consisted of 1 M $LiPF_6$ in a 1:1:1 (by volume) mixture of dimethyl carbonate (DMC), diethyl carbonate (DEC), and ethylene carbonate (EC). In a high-purity argon glove box (H_2O and O_2 <0.1 ppm), the CR2025 coin cells were fabricated with lithium metal employed as counter/reference electrode. The cells were tested using a LAND testing system for galvanostatic charge–discharge cycling (0.01–3.0 V), long-term cycling stability and rate capability. Cyclic voltammetry (CV) of the working electrode was executed on a CHI 660E electrochemical workstation (Shanghai Chenhua Instrument Co., Ltd.) at 0.1 mV/s. Electrochemical impedance spectroscopy (EIS) was performed on an AMETEK 1260A workstation (Advanced Measurement Technology, Inc.) at open circuit potential with an amplitude of 5 mV and a frequency range of 100 kHz to 0.01 Hz.

3. RESULTS AND DISCUSSION

In an alkaline environment, chitosan reacts with chloroacetic acid. This results in the initial stage of carboxymethylation occurring at the C6 position of the primary alcohol group. The introduction of these groups creates highly polar, water-soluble, carboxylate-based structures. The resulting material is vacuum-dried and used as CMCS powder, the is presented in Scheme 1a. The strong adsorption properties of water-soluble, carboxylated chitosan towards Fe^{3+} and Ni^{2+} ions mean that introducing these ions enhances the redox reactions that occur during the formation of electrode materials, thereby improving their electrochemical performance. Using carboxylated chitosan as a carbon source enables the creation of three-dimensional, interconnected, porous carbon, which helps buffer mechanical strain during cycling. The nitrogen alters electron density and active sites, and generates defects. This enhances the interaction between lithium (Li) and nitrogen (N), thereby improving the material's chemical adsorption capacity for lithium ions (Li^+). The $Fe_{0.64}Ni_{0.36}$@C-N nanocomposite was prepared via direct pyrolysis using the method shown in Scheme 1b. Microwave heating eliminates temperature gradients, making the -$COO^-$and -NH_2 groups in CMCS molecules more fully exposed, thereby improving the utilization rate of coordination sites and shortening the reaction time. Meanwhile, the non-thermal effect promotes the uniform nucleation of iron and nickel crystals. Scheme 1c shows the electrochemical cycle performance of FN2, FN6, FN10, FN14 and CMCS electrodes at 1 A g^{-1}. The as-prepared FN6 anode displays an initial specific capacity of 1460 mA h g^{-1}, which represents the highest reversible capacity among all the samples.

XRD is employed to investigate the effect of distinct levels of carboxyl chitosan on the material structure. Figure 1a shows different X-ray diffraction profiles obtained for samples subjected to heat treatment. The XRD diffraction pattern of 2 ~ 14 mol L^{-1} CMCS after calcination at 800°C. The pattern shows a crystalline peak at 2θ = 11.53°, 23.28°, 34.56°, 39.01°, 46.43°, 60.28°, 61.25° and 65.24° corresponding to the $Ni_{5.64}Fe_{2.36}(OH)_{16}(CO_3)1.18!7.52H_2O$ plane of a nickel ferrite complex (JCPDS card 51–0463). The peaks at 2θ = 43.60°, 50.79°, 74.68° correspond to the (111), (200), (220) planes of the hexagonal lattice system of $Fe_{0.64}Ni_{0.36}$ (JCPDS card 47-1405). The 6 mol L^{-1} CMCS (FN6) diffractogram also showed the formation of the $Fe_{0.64}Ni_{0.36}$@graphite structure with peaks at 2θ = 43.60°, 50.79°, 74.68° corresponding to the (111), (200), (220) planes of the hexagonal lattice system of $Fe_{0.64}Ni_{0.36}$ (JCPDS card 47-1405) [21]. The peaks at 2θ = 26.43° correspond to the lattice planes of the cubic graphite system (JCPDS card 12–0212). CMCS is shown as a broad diffraction band, suggesting that the sample is amorphous carbon. It can be observed that the CMCS exhibits favourable properties in the reduction of iron and nickel alloys. Consequently, the composition and phase of the sample can be tailored by tuning the doping ratio of CMCS.

Raman spectroscopy was performed to confirm the degree of graphitization and imperfections of the samples. FN6 was selected as the representative sample. As exhibited in Fig. 1b, CMCS and FN6 nanocomposites have two characteristic peaks that correspond to the D band (~ 1350 cm^{-1}) and G (~ 1580 cm^{-1}) with an intensity ratio (I_D/I_G) of 1.06 and 1.01, respectively[22]. The G peak is consistent with

sp^2 C-C bonding and the D peak reveals structural defects for the ideal graphite sheets[23], respectively. The higher I_D/I_G ratio is attributed to N doping, which enhances the defects and disorder of carbon materials, and this is favorable for Li^+storage[24]. Meanwhile, the addition of iron and nickel leads to a decrease in the I_D/I_G ratio reflecting carbon crystallinity, indicating that Fe and Ni can catalyze the growth of graphene at high temperatures.

As revealed by SEM images (Fig. 2a), the obtained FN6 hallmark a reticular shape interlinked by porous carbon. As illustrated in Fig. 2b, the rough surface of the FN6 electrode suggests that the FeNi nanoparticles are tightly confined within carbon layers, which is favorable for enhancing structural stability, enriching active sites, and improving the electrical conductivity of the sample. As revealed by HRTEM image (Fig. 2c and Fig. 2d), the FeNi surface is uniformly coated with a thin amorphous carbon layer. As shown in Fig. 2d, a lattice spacing of 0.26 nm is measured, which is consistent with the (111) crystal plane of $Fe_{0.64}Ni_{0.36}$.

XPS results revealed the detailed elemental binding configuration of FN6, and the corresponding elemental contents of O 1s, C 1s, Fe 2p, N 2p, and Ni 2p (Fig. 3a). As shown in Fig. 3b, the Ni 2p spectrum has been split into two main peaks at $2p_{3/2}$ (856.3 eV) and $2p_{1/2}$ (874.1 eV), indicating the successful doping of the Ni atoms into the carbon coating layer of the FN6 composite. The Fe 2p spectrum (Fig. 3c) exhibits peaks at binding energies of 712.5 eV and 726.4 eV, corresponding to the $2p_{3/2}$ and $2p_{1/2}$ components of Fe^0, respectively. In addition, a strong O 1s peak appeared in the XPS spectrum (Fig. 3d), which could be ascribed to the presence of Fe and Ni in the forms of oxygen-containing functional groups. As shown in Fig. 3e, the XPS spectrum of N 1s distinctly demonstrates the existence of graphitic-N (401.4 eV), pyrrolic-N (400.1 eV), pyridinic-N (398.2 eV), further confirming the N components in FN6. Moreover, graphite N exhibits a high electrical conductivity for electrode material, while the pyrrolic N and pyridinic N can enhance the electron-donating capability of the electrode material, due to the abundant Li^+ storage sites in FN6[25]. As can be seen from Fig. 3f, the C 1s spectrum exhibits four main peaks at binding energies of 284.7, 285.9, 286.6, and 289.7 eV, which are assigned to C-C/C-H, COOH/COOR, C-N/C-O, and O = C-O bands, respectively.

As shown in Fig. 4a, the charge/discharge rate performance of the FN2, FN6, FN10, FN14, and CMCS electrodes (tested between 0.01 and 3.0 V) was evaluated at various current densities ranging from 0.05 to 1.0 A g^{-1}, followed by a return to 0.05 A g^{-1}. Notably, the specific discharge capacity of FN6 electrode reaches 890 mAh g^{-1} when the current density returns to 0.05 A g^{-1}, implying the FN6 electrode is apparently superior to those of the FN2, FN10, FN14 and CMCS electrodes (Fig. 4b). To clearly reveal the delithiation and lithiation processes in the FeNi nanocomposites as LIBs anodes, the cyclic voltammogram (CV) of FN6 was obtained under a voltage range of 0.01-3.0 V (vs.Li/Li^+) for the first three cycles at 0.1 mV s^{-1}. As illustrated in Fig. 4c, four main peaks located at 0.61, 0.95, 1.58 and 2.52 V in the first cycle. During the anodic process, the peaks around 0.73 V and 1.37 V correspond to the oxidation of Fe^0 and Ni^0 into Fe^{3+} and Ni^{2+}. During cathodic process, the peaks located at 1.58 V and 2.52 V are ascribed to the reduction of Ni^{2+} and Fe^{3+} to metallic Ni^0 and Fe^0, respectively.

Figure 4d exhibits the relationship between potential and capacity of FN6 during charge/discharge process in the 1st, 2nd, and 3rd cycles at 0.05 A g^{-1} within a potential window of 0.01-3.0 V (vs.Li/Li^+). The initial discharge capacity reaches 1181.1 mAh g^{-1}, accompanied by a Coulombic efficiency of 67.77%. The pronounced irreversible capacity loss during the first cycle can be ascribed to the formation of the solid electrolyte interface (SEI) film. The Coulombic efficiency gradually approaches and stabilizes at nearly 90% in the 2nd and 3rd cycles, implying the progressive stabilization of the SEI layer. It is worth noting that no obvious charge/discharge plateaus are observed, which can be attributed to the multivalent evolution of Ni, Fe, and N during the generation of resultant products. This is likely attributed to the incomplete reaction and the formation of the SEI layer. For the subsequent charge/discharge curves, several plateaus appear at approximately 1.37 V in the charge profiles and 2.52 V in the discharge profiles, consistent with the CV analysis in Fig. 4c.

Figure 4e demonstrates the rate performance of FN2, FN6, FN10, FN14 and CMCS electrodes. The FN6 electrode exhibits average specific discharge capacities of 915, 837, 793, 698 and 576 mAh g^{-1} at various current densities of 0.05, 0.1,0.2, 0.5 and 1.0 A g^{-1}, respectively. Impressively, the FN6 electrode delivers a high specific discharge capacity of 878 mAh g^{-1} when the current density is returned to 0.05 A g^{-1}, exhibiting outstanding rate performance. The capacity improvement can be ascribed to the carbon coating layer, which provides abundant active sites and pore channels for lithium-ion storage. Figure 4f shows the cycle stability of the as-prepared electrodes at 1.0 A g^{-1}. The specific capacities of FN2, FN6, FN10, FN14 and CMCS electrodes are 54.6, 279.3, 161.6, 256.1 and 52.5 mAh g^{-1} after 1000 cycles, with associated capacity retention rates of 12.9%, 47.5%, 35.6%, 80.8% and 55.4%, respectively. Among the five electrodes, the FN2 electrode only achieves a relatively low capacity retention, suggesting that the mass percentage of C is conducive to the improvement rate performance. Among the five electrodes, the FN2 electrode exhibits a low capacity retention, implying that carbon content plays a key role in boosting rate capability. Furthermore, the C content for FN6 is less than FN10, but its specific capacity is higher than that of FN10. Furthermore, despite having a lower carbon content than FN10, the FN6 electrode delivers a higher specific capacity, indicating that a moderate carbon content is favorable for capacity enhancement. The FN14 shows the best capacity retention rate after 1000 cycles at 1 A g^{-1}. As summarized in Table 1, the discharge capacities of the five anode materials reveal that FN14 exhibits superior cycling stability relative to FN6. In this paper, the exceptional cycling stability and rate capability of $Fe_{0.64}Ni_{0.36}$@C-N nanocomposites can be attributed to the following factors: i) the carbon can effectively mitigate structural stress and volume expansion during charge/discharge process; ii) $Fe_{0.64}Ni_{0.36}$ can suppress the formation of lithium dendrites and effectively improve the electrochemical stability[26]; iii) the heterostructure can enhance electrochemical performance via a favorable synergistic interaction between $Fe_{0.64}Ni_{0.36}$ and C, N co-dopants. Furthermore, the carbon not only enhances electrical conductivity of the electrode but also facilitates the transportation of Li^+, thereby contributing to a high capacity[27].

Table 1
Comparison of specific capacities of various anode materials

Anode materials	Initial discharge Capacity (mAh g^{-1})	Capacity after 1000 cycles at 1 A g^{-1} (mAh g^{-1})	Capacity retention rate
FN2	423.9	54.6	12.9
FN6	587.6	279.3	47.5
FN10	453.5	161.6	35.6
FN14	316.9	256.1	80.8
CMCS	94.7	52.5	55.4

To further determine the superior electrochemical performance of FN6 electrode, the CV tests for various scan rates are performed. As shown in Fig. 5a, the CV curves for the FN6 electrode display similar profiles at various scan rates, suggesting consistent electrochemical reactions upon cycling. The relationship between the peak current (*i*) and scan rate (*v*) follows the power-law equation[28]

$$i = av^{b} \quad (1)$$

In which, the value of *b* is obtained from the slope of log(*i*) against log(*v*)[29]. Generally, when *b* is 1.0 and 0.5, the lithium storage is mainly controlled by pseudocapacitive and diffusion behavior, respectively[30, 31]. For the FN6 electrode, Fig. 5b displays the b values of peak A (0.79759) and peak B (0.8791) are close to 1.0, suggesting that the lithium-ion storage process is controlled by a pseudocapactive process. Additionally, the capacity proportions of pseudocapacitive processes and diffusion-controlled at various scan rates can be further determined by Eq. (2)[29, 32] :

$$i=k_{1}v+k_{2}v^{1/2} \quad (2)$$

Where k_1v and $k_2v^{1/2}$ represent the contributions of diffusion-controlled and pseudocapacitive, respectively. In Fig. 5c, the contribution rates of diffusion- controlled process are 62.37%, 64.84%, 71.78%, 77.29%, 80.83% and 83.54% at the scan rates of 0.1, 0.2, 0.4, 0.6, 0.8 and 1.0 mV s^{-1}, respectively. In this work, the Li storage capacity of FN6 is dominated by diffusion-controlled process at different scan rates of 0.1 ~ 1.0 mV s^{-1}. For FN6, the pseudocapacitive proportion at 0.4 mV s^{-1} is shown in Fig. 5d, delivering a high contribution rate (red region) of 71.78% to the total storage capability. It can be found that the excellent rate performances, superior cycling stability and high specific capacity of $Fe_{0.64}Ni_{0.36}$ can be ascribed to the synergistic interaction between various heterostructured components.

To fully analyze the electrochemical reaction kinetics of FN2, FN6, FN10 and FN14 electrodes, we performed EIS spectra, as shown in Fig. 6a. Obviously, all of the spectra comprise an inclined line in the low-frequency region and a semicircle in the high-frequency region[33]. Furthermore, the EIS spectra can

be fitted with equivalent circuit diagrams in Fig. 6b, in which, Rct, Rs, CPE and W represent charge transfer resistance, electrolyte resistance, double layer capacitance and Warburg impedance, respectively[34]. Additionally, a gradual reduction in semicircle diameter is observed for FN2, FN6, FN10, and FN14 electrodes in the high-frequency range, which confirms the improved charge-transfer kinetics and decreased impedance. Furthermore, the sloped line in the low-frequency region corresponds to the impedance of lithium-ion diffusion within the sample. The diffusion coefficient of Li^+ (D_{Li}) was calculated using Eqs. (3) and (4)[35].

$$D_{Li} = \frac{R^2T^2}{2A^2n^4F^4C^2\sigma^2} \quad (3)$$

$$Z' = R_s + R_{ct} + \sigma\omega^{-0.5} \quad (4)$$

Table 2. The σ and D_{Li} of various anode materials.

Anode materials	σ ($\Omega\ s^{-0.5}$)	D_{Li} ($cm\ s^{-1}$)
FN2	174.7	1.20E-14
FN6	83.3	5.26E-14
FN10	21.4	7.97E-13
FN14	18.5	1.07E-12

In which, T = 298.15 K, A (electrode area) = 1.54×10^{-4} m^2, R (gas constant) = 8.314 J k^{-1} mol^{-1}, F(Faraday constant) = 96,485C mol^{-1}, C stands for the concentration of lithium ions and n represents the transferred electrons number during conversion of per mole (i.e., $NiFe_2O_4$, n = 8). Figure 6c exhibits the graph of Zre plotted against $\omega^{-0.5}$. The σ value of FN2, FN6, FN10 and FN14 electrodes is 174.7, 83.3, 21.4, and 18.5 Ω $\omega^{-0.5}$, respectively. The D_{Li} of FN2, FN6, FN10 and FN14 anode electrodes are shown in Table 2. This can prove that the anode materials for the FN6 possess better lithium-ion diffusion ability and lower charge transfer impedance.

4. CONCLUSIONS

In summary, the FeNi nanoparticles with different contents of CMCS have been prepared via a microwave-assisted sol-gel process. It is found that the CMCS content in the nanocomposites plays a crucial role in further improving electrochemical performance of the FeNi@C electrode. When the CMCS content increases to 6 mol L^{-1}, FeNi nanoparticles were successfully encapsulated by carbon networks. The FN6 electrode displays good rate capability as anode materials for Lithium ion batteries. The improved anode performance arises from the synergistic effect between the $Fe_{0.64}Ni_{0.36}$ nanoparticles and the carbon layer flakes. The carbon layer can reduce the resistance and increase the specific surface area, thus facilitating the lithium-ion diffusion. When the CMCS content was increased to 14 mol L^{-1}, the FN14 electrode demonstrated superior cycling stability. During the material synthesis process, the microwave promotes the formation of FeNi nanoparticles and also favors the generation of a porous carbon layer, which enhances lithium-ion diffusion. The microwave-assisted sol-gel method is energy-saving with a short reaction time, and thus holds great potential for widespread application. Meantime, many challenges remain in optimizing the microwave-assisted sol-gel process through molecular design theory to achieve both superior cycling stability and high rate capability simultaneously. In general, the FeNi nanocomposites display significant potential as anode candidates for high-performance Lithium-ion batteries.

Declarations

Author Contribution

R.B. Yao, C.X. Sun, and M.Y. Wang, D.Y. Zheng wrote the main manuscript text. Y.H. Zheng and J.H. Zhu prepared Figures 1–4, while C. Liu and G.T. Guo were responsible for Figures 5 and 6. All authors reviewed the manuscript.

ACKNOWLEDGMENTS

The authors gratefully acknowledge the financial support from the National Natural Science Foundation of China (51377047), Jiangsu Province Distinguished Teaching Master Support Program, and the Lianyungang City Science and Technology Plan Project (CG2433, JC2503).

- **AUTHOR INFORMATION**

Notes

The authors declare no competing financial interest.

References

1. P. Simon, Y. Gogotsi, Perspectives for electrochemical capacitors and related devices. Nat. Mater. **19**, 1151-1163 (2020)

2. L. Liu, P.-L. Taberna, B. Dunn, P. Simon, Future directions for electrochemical capacitors. ACS Energy Lett. **6**, 4311-4316 (2021)
3. F. Wu, J. Maier, Y. Yu, Guidelines and trends for next generation rechargeable lithium and lithium-ion batteries. Chem.Soc.Rev. **49**, 1569–1614 (2020)
4. H. Yu, H. Fan, B. Yadian H. Tan, W. Liu, H.-H. Hng, Y. Huang, Q. Yan, General approach for MOF-derived porous spinel AFe_2O_4 hollow structures and their superior lithium storage properties. ACS Appl. Mater. Interfaces. **7**, 26751-26757 (2015)
5. G. Liu, J. Wang, X. Sheng, X. Xue, Y. Wang, Thermodynamics and electronic structure characteristics of MFe_2O_4 with different spinel structures: a firstprinciples study.Ceram. Int. **49**, 29747-29754 (2023)
6. H.-W. Park, K.-C. Roh, Recent advances in and perspectives on pseudocapacitive materials for supercapacitors-A review.J. Power Sources. **557**, 232558 (2023)
7. S. Mahadik, S. Surendran, J.-Y. Kim, G. Janani, D.-K. Lee, T.-H. Kim, U. Sim, Structurally engineered Ni-Fe based nanocomposites with carbonaceous interlayers for advanced Li-ion storage. J. Mater. Chem. A. **10**, 14655-14673 (2022)
8. M.-S. Shruti, A. Sasmal, H. HyukSu, A.-K. Nayak, High-performance supercapacitor based on self-heteroatom-doped porous carbon electrodes fabricated from Mikania micrantha. Mater. Chem. Phys. **314**, 128826 (2024)
9. A.-K. Nayak, A.-K. Das, D. Pradhan, Carbon-supported $NiFe_2O_4$ nanofibers for high-performance Lithium-ion batteries. ACS Sustainable Chemistry & Engineering. **5**, 10128-10138 (2017)
10. D.-G. Wang, Z. Liang, S. Gao, C. Qu, R. Zou, Metal-organic framework-based materials for hybrid supercapacitor application. Coord. Chem. Rev. **404**, 213093 (2020)
11. L. Abbasi, M. Arvand, S.-E. Moosavifard, High-performance supercapacitor electrode based on $NiCo_2O_4$ nanospheres decorated multi-walled carbon nanotubes. Carbon.**161**, 299-308 (2020)
12. T. Di, S. Na, Z. Mengxiao, L. Xiaofeng, W. Ce, Rational design of hierarchical Ni-Co-S nanosheet arrays on Ni foam for high-performance hybrid supercapacitors. ACS Appl. Mater.Interfaces.**12**, 1280-1291 (2020)
13. Y. Gao, L. Zhao, Coaxial nickel cobalt selenide/nitrogen-doped carbon nanotube array as a three-dimensional self-supported electrode for electrochemical energy storage. Chemical Engineering Journal.**430**, 132745 (2022)
14. Wang, X. H. Song, S. Ma, M. Li, G. He, M. Xie, X. Guo, Design of carbon-based composite electrodes for enhanced electrochemical energy storage performance. Chemical Engineering Journal. **432**, 134319 (2022)
15. R. Zhang, J. Dong, W. Zhang, L. Ma, Z. Jiang, J. Wang, Y. Huang, CoOx@NiMoN/Ti_3C_2T interface for stable high-performance electrochemical energy storage devices. Nano Energy. **91**, 106633 (2022)
16. L. Abbasi, M. Arvand, S.-E. Moosavifard, Facile template-free synthesis of 3D hierarchical ravine-like interconnected $MnCo_2S_4$ nanosheet arrays for hybrid energy storage devices. Carbon.**161**, 299-308

(2020)

17. K. Chhetri, T. Kim, D. Acharya, A. Muthurasu, B. Dahal, R.-M. Bhattarai, H.-Y. Kim, Hollow carbon nanofibers with inside-outside decoration of bi-metallic MOF derived Ni-Fe phosphides as electrode materials for asymmetric supercapacitors. Chem. Eng. J. **450**, 138363. (2022)
18. T. Li, S. Fu, L. Ma, Y. Yang, T. Wu, S. Wei, W. Zhan, Facile synthesis of N-doped carbon nanotubes decorated with $NiCo_2O_4$ nanoparticles for high-performance supercapacitors. J. Mater. Sci.-Mater. Electron. **33**, 22319-22331 (2022)
19. V.-K. Mourya, N.-N. Inamdar, A. Tiwari, Carboxymethyl chitosan and its applications. Adv. Mater. Lett. **1**, 11-33 (2010)
20. R. Czechowska-Biskup, R. Wach, P. Stojek, M.Kamińska, J.-M. Rosiak, P. Ulański, Chitosan-based materials for electrochemical energy storage applications. Prog. Chem. Appl. Chitin.**21**, 27-45 (2016)
21. D.-Y. Zheng, R.-B. Yao, C.-X. Sun, J.-L. Li, Y.-H. Zheng, J.-H. Zhu, C. Liu, Fe-Ni with chitosan via microwave and carboxymethyl as electrode materials for supercapacitor. ChemNanoMat. **11**, 202400594. (2025)
22. J. Zhang, Z. Yang, J. Qiu, H-W. Lee Design and synthesis of nitrogen and sulfur co-doped porous carbon via two-dimensional interlayer confinement for a high-performance anode material for lithium-ion batteries. J Mater Chemistry A. **4**, 5802-5809 (2016)
23. MSAS. Shah, J. Lee, AR. Park, Y. Choi, W-J. Kim, J. Park, C-H. Chung, J. Kim, B. Lim, PJ. Yoo, Ultra-fine SnO_2 nanoparticles doubly embedded in amorphous carbon and reduced graphene oxide (rGO) for superior lithium storage. Electrochim Acta. **224**, 201-210 (2017)
24. Z. Qiu, Y. Lin, H. Xin, P. Han, D. Li, B. Yang, P. Li, S. Ullah, H. Fan, C. Zhu, Ultrahigh level nitrogen/sulfur co-doped carbon as high performance anode materials for lithium-ion batteries. Carbon. **126**, 85-92 (2018)
25. H. Li, Z. Wang, L. Dang, K. Yu, R. Yang, A. Fu, X. Liu, Y.-G. Guo, H. Li, Precursor induced assembly of Si nanoparticles encapsulated in graphene/carbon matrices and the influence of Al_2O_3 coating on their properties as anode for Lithium-ion batteries. Small. **20**, 2307722. (2024)
26. Z. Yu, J. Zhou, X. Lv, C. Li, X. Liu, S. Yang, Y. Liu, Nitrogen-doped porous carbon nanofiber decorated with FeNi alloy for dendrite-free high-performance lithium metal anode. J. Alloys Compd. **925**,166691. (2022)
27. G. Xiao, W. Cai, L. Zhu, Y. Fang, H. Ao, Y. Zhu, Y. Qian, N-Doped carbon nanotubes decorated with Fe/Ni sites to stabilize lithium metal anodes. Inorg. Chem. Front. **7**, 2747-2752. (2020)
28. 28. M. Vincent, V.-S. Avvaru, M. Haranczyk, V. Etacheri, Fast-charging and long-lasting Mg-Na hybrid batteries based on extremely pseudocapacitive bronze TiO_2 nanosheet cathodes, Chem. Eng. J. **433** 133810. (2022)
29. A.-Y. Shenouda, H. Liu, Electrochemical behaviour of tin borophosphate negative electrodes for energy storage systems. J. Power Sources. **185**, 1386-1391. (2008)

30. M. Vincent, S.-S. Kumar, D. Kowalski, Pseudocapacitive vs diffusion controlled charge storage in Fe_2O_3 nanosheet Na-ion battery. Electrochim. Acta.**469**, 143161. (2023)
31. Y. Tang, L. Liu, H. Zhao, Y. Zhang, L. Kong, S. Gao, X. Li, L. Wang, D. Jia, Pseudocapacitive behaviors of Li_2FeTiO_4/C hybrid porous nanotubes for novel lithium-ion battery anodes with superior performances. ACS Appl. Mater. Interfaces, **10**, 20225-20230 (2018)
32. J.-H. Moon, H. Seong, G. Kim, Y. Jin, H. Yoo, T. Jung, C. Lee, M.Yoon, K.-T.Lee, J. Choi, Synthesis and electrochemical properties of a superior capacity Bi_2S_3@rGO hybrid composite used as an anode for Lithium-ion batteries. Energy Fuels. **39**, 1432–1439 (2025)
33. P. Periyannan1, A.-M. Musthafa, S. Masilamani, Synergistic Design of $LiMn_{0.5}Fe_{0.5}PO_4$/C Composites for HighPerformance Lithium-Ion Batteries. Journal of Inorganic and Organometallic Polymers and Materials. **35**. 8175-8185 (2025)
34. F. Xie, X. Sheng, Z. Ling, S. Hao, Q. Zhang, M. Sun,G. Liu, F. Diao, Y.-Q. Wang, Flexible electrospun iron/manganese-based compounds/carbon fibers: phase transformation and electrochemical properties. Electrochim. Acta. **470**, 143288 (2023)
35. M. Sun, Z. Cui, H. Liu, S. Li, Q. Zhang, X. Sheng, Y.-Q. Wang, Graphene-wrapped FeOOH nanorods with enhanced performance as lithium-ion battery anode. NANO. **16**, 2150005 (2021)

Scheme 1

Scheme 1 is available in the Supplementary Files section.

Figures

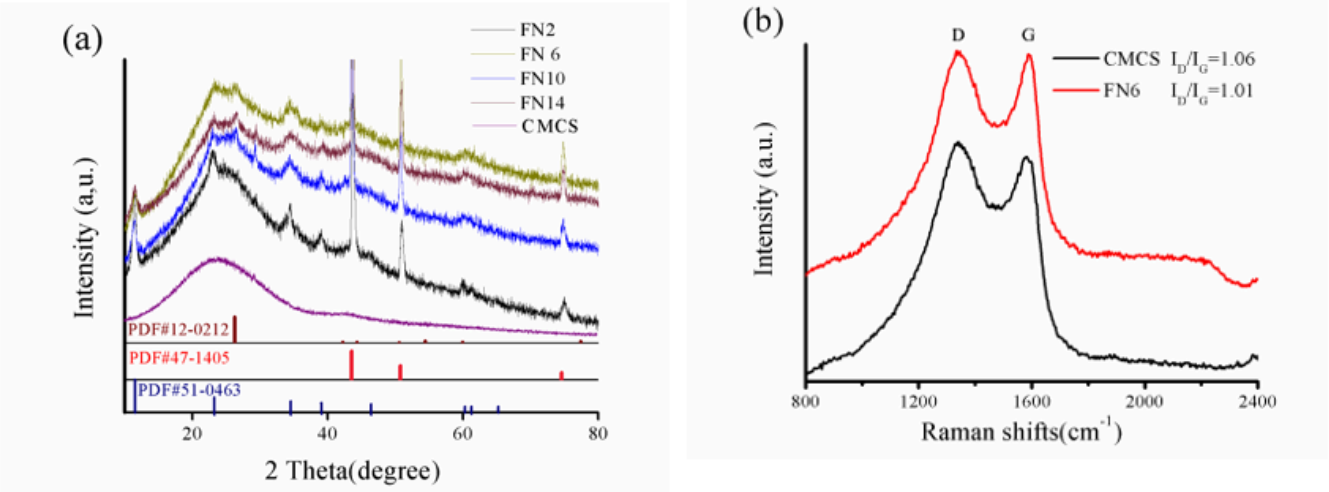

Figure 1

(a) XRD patterns of samples for FN2, FN6, FN10, FN14 and CMCS; (b) Raman D and G bands of CMCS and FN6 anode materials.

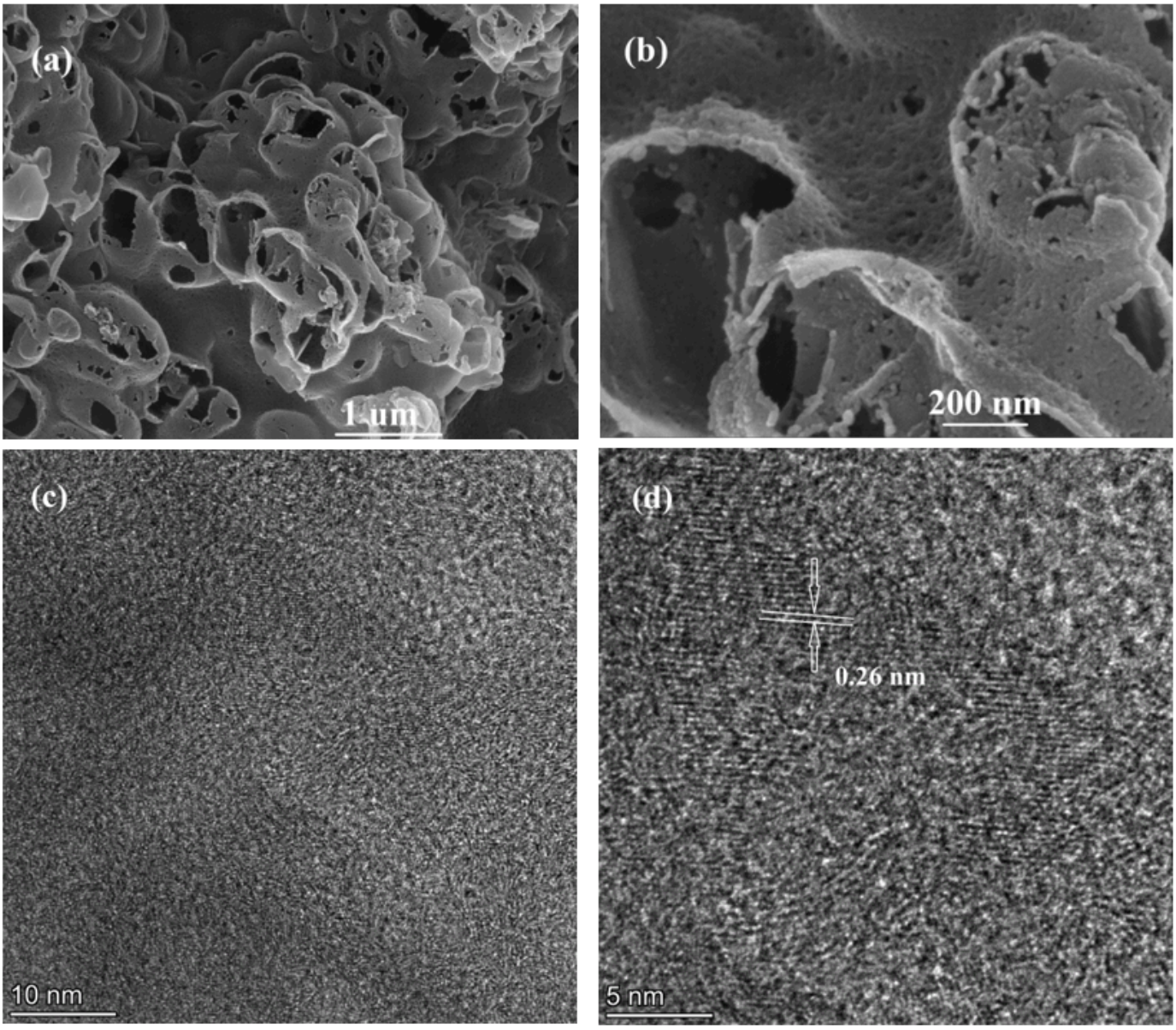

Figure 2

SEM images of FN6 (a, b), high-resolution TEM (HRTEM) images of FN6 (c, d).

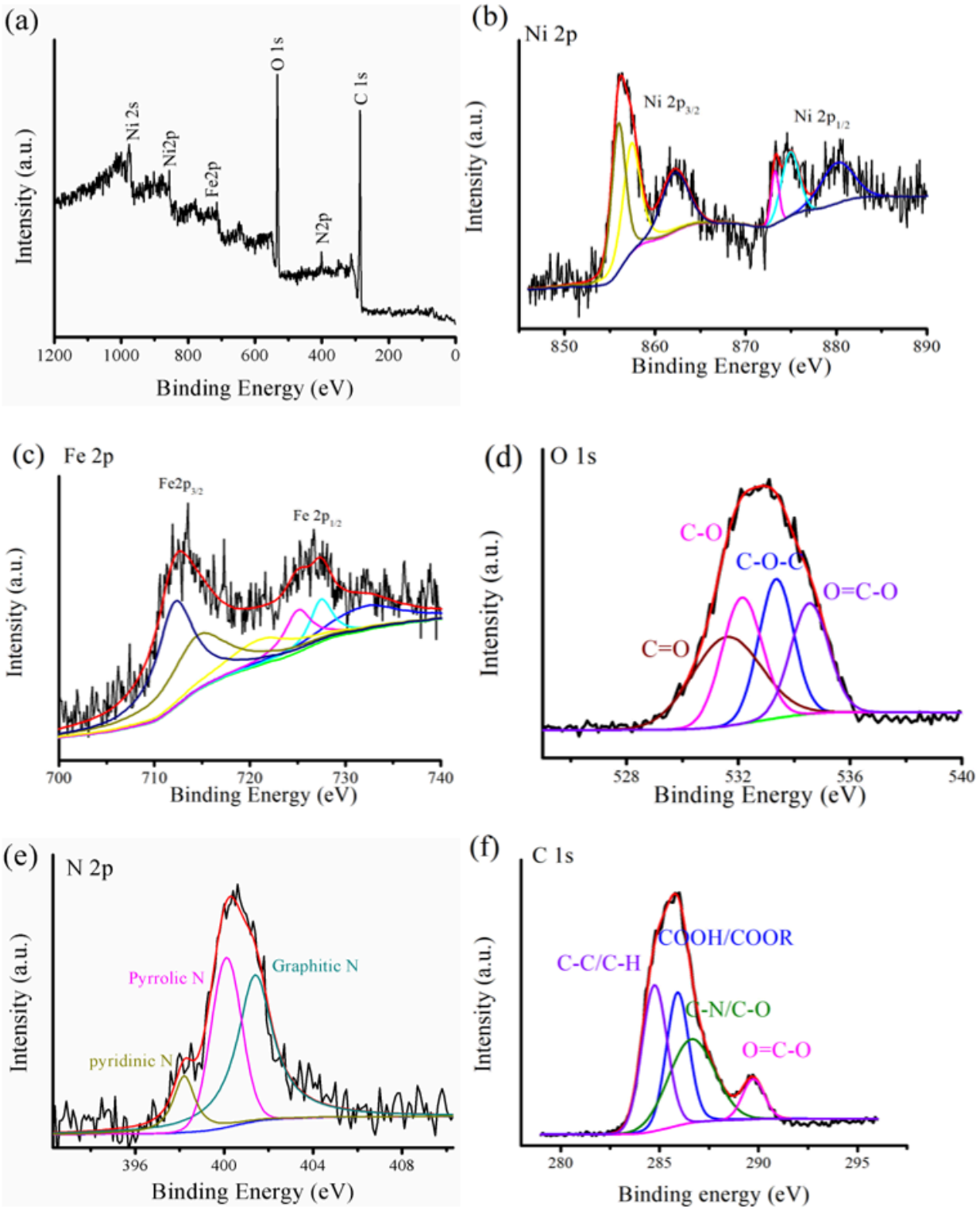

Figure 3

XPS survey spectra of FN6. (a) total survey spectrum; (b) Ni 2p; (c) Fe 2p; (d) O 1s (e) N 2p and (f) C 1s.

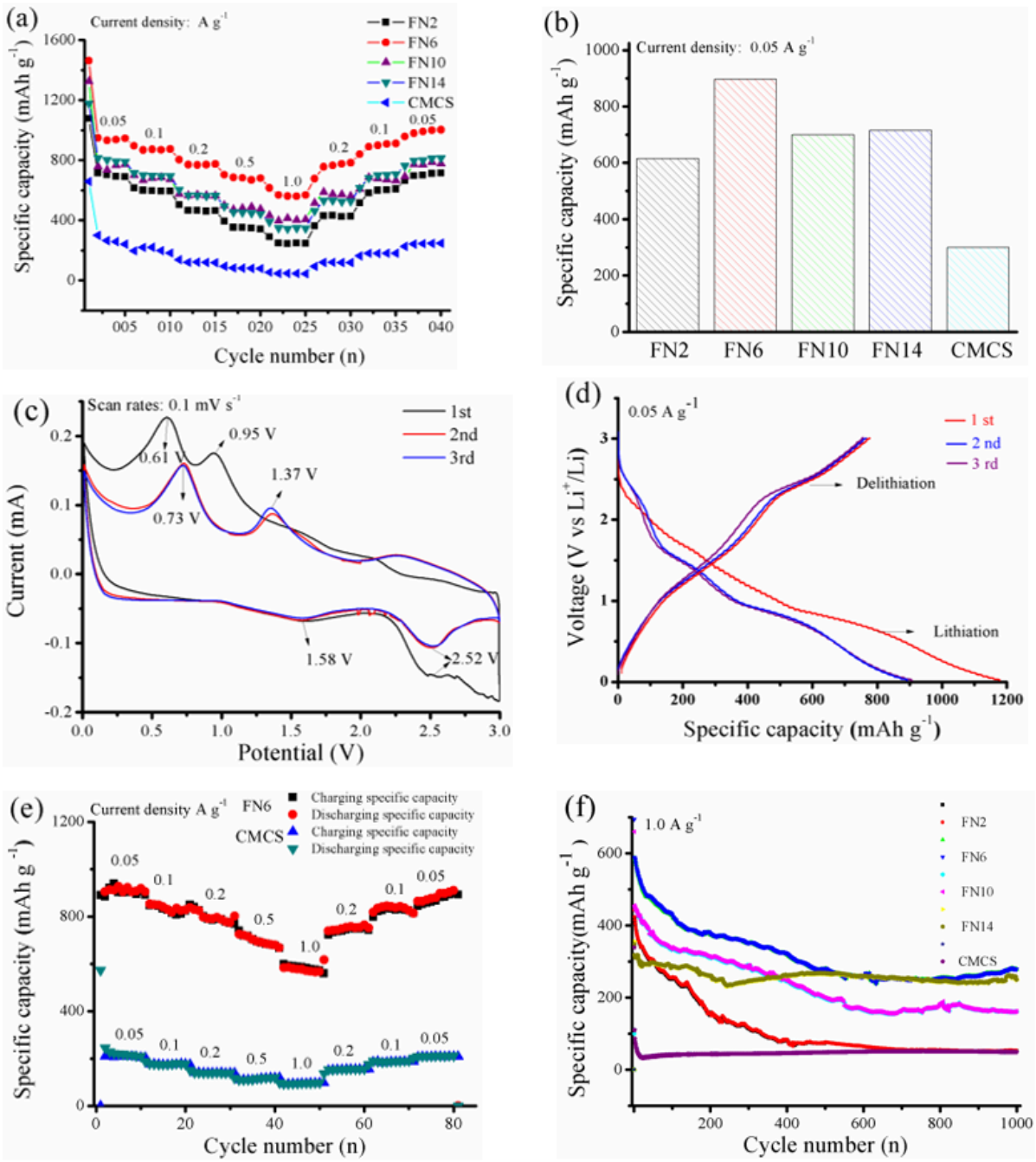

Figure 4

Electrochemical performances of the electrode materials: (a) comparison of rate performance at various current densities of FN2, FN6, FN10, FN14 and CMCS. (b) comparison of rate performance of FN2, FN6, FN10, FN14 and CMCS at 0.05 A g^{-1}. (c) Cyclic voltammograms (CVs) for FN6 electrode at the first three cycles at 0.1 mV s^{-1}. (d) The charge/discharge voltage curves of FN6 from the 1st cycle to the 3rd cycle at 0.05 A g^{-1}. (e) Rate performance at different current densities, and (f) Long-term cycling performance at a current density of 1.0 A g^{-1} for 1000 cycles.

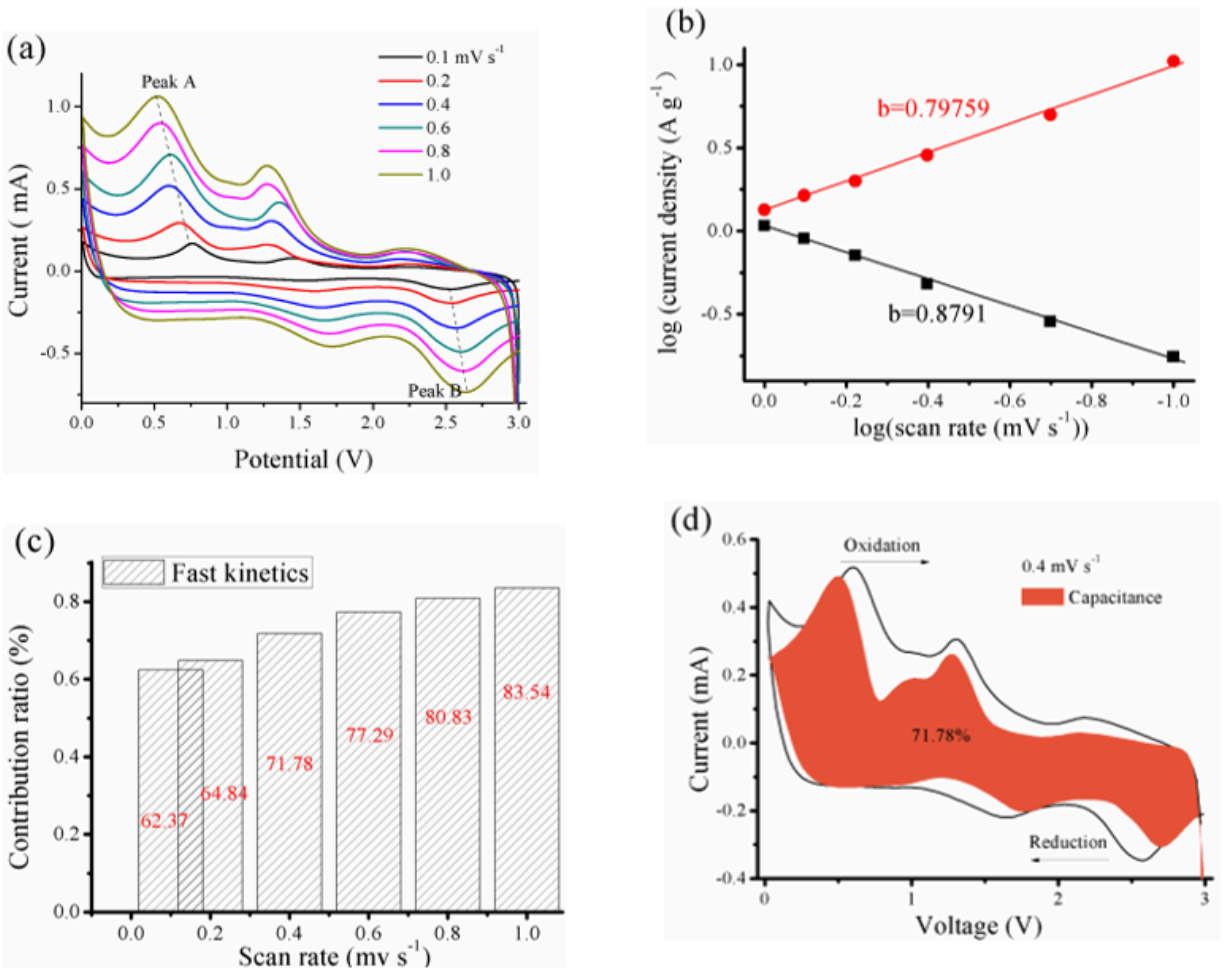

Figure 5

(a) CV curves of FN6 at different scan rates. (b) The b (slope) values of FN6. (c) Diffusion-controlled contribution of FN6 within 0.1–1.0 mV/s. (d) Corresponding capacitive contribution of FN6 at 0.4 mV s^{-1}.

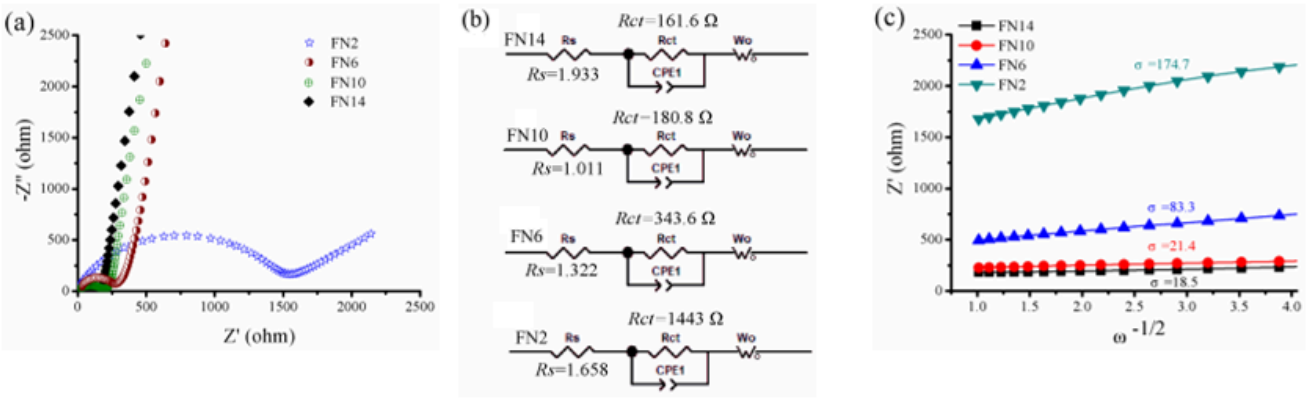

Figure 6

(a) Electrochemical impedance spectra of the FN2, FN6, FN10 and FN14 electrodes. (b) Equivalent electrical circuit model. (c) Graph of $Z^{/}$ plotted against $\omega^{-0.5}$.

Supplementary Files

This is a list of supplementary files associated with this preprint. Click to download.

- Scheme1.docx